Research Square

Preprints are preliminary reports that have not undergone peer review.
They should not be considered conclusive, used to inform clinical practice,
or referenced by the media as validated information.

Multimodal imaging characterization of structural phenotypes and biomarkers in choroidal hemangioma associated with Sturge–Weber syndrome

Serena Fragiotta
Sapienza University of Rome
Mariachiara Di Pippo
Sapienza University of Rome
Chiara Ciancimino
Sapienza University of Rome
Francesco Rispoli
Sapienza University of Rome
Gianluca Scuderi
Sapienza University of Rome
Solmaz Abdolrahimzadeh
solmaz.abdolrahimzadeh@uniroma1.it
Sapienza University of Rome

Research Article

Keywords:

Posted Date: September 16th, 2026

DOI: https://doi.org/10.21203/rs.3.rs-10870553/v1

License: This work is licensed under a Creative Commons Attribution 4.0 International License.
Read Full License

Additional Declarations: No competing interests reported.

Abstract

Background

To identify and characterize microstructural alterations and biomarkers of diffuse choroidal hemangioma (DCH) associated with Sturge–Weber syndrome (SWS) using multimodal imaging.

Methods

This was a retrospective, observational study where sixteen eyes of 16 patients with SWS and DCH underwent a comprehensive clinical evaluation and a standardized non-invasive multimodal imaging protocol, including color fundus photography, near-infrared reflectance (NIR) and infrared (IR) imaging, fundus autofluorescence, and spectral-domain optical coherence tomography (SDOCT). Microstructural alterations across the neurosensory retina, retinal pigment epithelium (RPE), and choriocapillaris were qualitatively graded by independent masked experts and correlated with choroidal subfoveal thickness (CSFT) and clinical parameters.

Results

Multimodal imaging identified four distinct microstructural phenotypes. The most frequent finding was hyperreflective dots, seen in 81.25% (13/16) of eyes as round-to-angular hyperreflective structures on NIR/IR imaging. Inner retinal folds appeared in 37.5% (6/16) of eyes as undulations and irregularities affecting the internal limiting membrane and retinal nerve fiber layer. Drusenoid-like lesions, characterized by granular hyperreflectivity localized between the ellipsoid zone and the RPE, resembling subretinal drusenoid deposits, were observed in 31.2% (5/16) of eyes. A demarcation line was seen as a linear or curved hyperreflective line on NIR in 18.75% (3/16) of eyes.

Discussion

DCH in SWS is characterized by a specific spectrum of secondary structural remodeling at the chorioretinal interface. These microstructural phenotypes likely reflect a combination of chronic mechanical strain from the underlying mass and localized tissue hypoxia due to an inefficient vascular environment, serving as valuable non-invasive biomarkers for tracking disease chronicity and monitoring disease progression.

Introduction

Sturge–Weber syndrome (SWS) is a rare, congenital neuro-oculocutaneous disorder classically characterized by a facial cutaneous capillary malformation (port-wine stain), ipsilateral leptomeningeal angiomatosis, and various ocular abnormalities[1–5].

Ocular involvement is common and represents a major cause of progressive visual loss, with secondary glaucoma and choroidal hemangioma (CH) serving as the most prevalent clinical manifestations[6]. While secondary glaucoma typically commands immediate therapeutic intervention due to the risk of irreversible optic neuropathy, choroidal manifestations often remain underdiagnosed, especially in their early stages[3, 5]. CH associated with SWS are predominantly diffuse choroidal hemangioma (DCH), occurring in 20–70% of syndromic patients[7]. These lesions are typically asymptomatic, presenting ipsilateral to the facial capillary malformation and observed clinically as a “tomato-ketchup” fundus appearance. However, this clinical presentation can be easily overlooked, making the diagnosis challenging[1, 6, 7]. DCH can lead to severe sight-threatening outcomes if complicated by neurosensory retinal detachment, subretinal fluid accumulation, and macular edema, alongside with outer retina and retinal pigment epithelium (RPE) alterations[3, 7–9].

To facilitate early recognition of DCH, our group recently established ophthalmic imaging criteria using multimodal, non-invasive technologies. According to this study, only 31% of patients were diagnosed using color fundus photography, whereas the combination of near-infrared reflectance (NIR) and enhanced depth imaging (EDI) spectral domain optical coherence tomography (SDOCT) achieved 100% sensitivity and accuracy [16]. While establishing primary diagnostic criteria is a critical step for early intervention, a significant gap remains regarding the microstructural alterations in the choriocapillaris, RPE, and neurosensory retina surrounding the vascular lesion[8, 10–14]. Histologically, these lesions are considered hamartomas composed of mature capillary proliferations and cavernous vascular channels. Histopathological studies have documented the progressive deterioration of the outer retina, RPE, and choriocapillaris.[14, 15].

These alterations may reflect the mechanical stress, chronic ischemia, and subsequent metabolic exhaustion of the RPE-photoreceptor complex. Changes that may significantly impact the long-term visual prognosis.

This retrospective, observational imaging study serves as an ancillary project to our previous diagnostic research. Its primary objective is to identify and characterize structural correlates of DCH secondary to SWS using multimodal imaging. Furthermore, to investigate the relationship between distinct structural phenotypes and clinical parameters, including visual function, choroidal subfoveal thickness (CSFT), and other clinical and demographic characteristics.

Material and methods

Study Design and Participants

This retrospective, observational imaging study is an ancillary project derived from a previously published investigation of non-invasive diagnostic imaging criteria for choroidal hemangioma in SWS[16]. The original cohort included patients recruited at the Retina Center of the Ophthalmology Unit,

Department of Neurosciences, Mental Health and Sensory Organs, Sapienza University of Rome, St. Andrea Hospital. The parent study was conducted in accordance with the Declaration of Helsinki, approved by the Ethics Committee of Sapienza University of Rome (approval code CE 7150/2023; approval date: 6 April 2023), and written informed consent was obtained from all participants or from parents/legal guardians in the case of minors.

A total of 17 patients presenting with a clinical diagnosis of SWS and suspected or confirmed underlying DCH were initially screened. Diagnosis of SWS was based on the presence of at least two of the following: leptomeningeal angioma, facial port-wine stain (nevus flammeus) typically in the trigeminal nerve distribution, and ocular involvement such as glaucoma or DCH. Patients with all three criteria were diagnosed as classic SWS, while the presence of 2 diagnostic criteria was classified as fruste form.

Inclusion criteria were high-quality multimodal retinal imaging, including color fundus photography (Optovue Solix, Optovue, CA, USA), NIR and SDOCT with Spectralis OCT + HRA (Heidelberg Engineering, Germany), OCT and OCT angiography performed with Solix device (Optovue Solix, Optovue, CA, USA), and infrared (IR) and fundus autofluorescence (FAF) obtained through Spectralis OCT + HRA (Heidelberg Engineering, Germany). Exclusion criteria consisted of severe media opacities (e.g. dense cataracts) precluding clear fundus visualization or adequate signal strength on imaging; co-existing posterior segment pathologies unrelated to SWS; poor patient cooperation during acquisition; and intraocular surgeries in the previous 6 months.

Clinical and Ophthalmologic Evaluation

All included patients underwent a comprehensive, standardized ophthalmological evaluation including best-corrected visual acuity (BCVA) using standard Early Treatment Diabetic Study (ETDRS) charts recorded as the number of letters read, and intraocular pressure measurement. Secondary glaucoma was diagnosed based on a documented history of elevated IOP (> 21 mmHg), characteristic glaucomatous optic neuropathy, corresponding visual field defects where testable, or ongoing use of anti-glaucoma medications. Slit-lamp biomicroscopy of the anterior segment and dilated fundus examination using binocular indirect ophthalmoscopy were performed on all eyes.

Multimodal Imaging Protocol

Retinal and choroidal structural architectures were analyzed using a multimodal imaging protocol. Non-invasive imaging was executed using the Spectralis HRA + OCT platform (Heidelberg Engineering, Heidelberg, Germany). Infrared reflectance (IR)/ NIR uses ~ 820–830 nm laser with confocal scanning laser ophthalmoscopy, penetrating deeper than visible light and enhancing outer retina, RPE, and choroid visualization[17–19]. IR was acquired with a standard 55° field, while FAF was obtained using an excitation wavelength of 488 nm solid-state laser and a barrier filter at 500 nm[20, 21].

En-face NIR images were acquired using a 30° × 30° field centered on the macula automatically during OCT B-scan acquisition. OCT B-scans were acquired using enhanced depth imaging (EDI-SDOCT) protocols to ensure optimized visualization of the deep choroidal and choriocapillaris layers. The B-scan protocol included high-resolution horizontal and vertical line scans across the fovea and papillomacular bundle, as well as a standardized volume scan consisting of at least 25 lines within a 20°×20° area centered on the lesion, when permitted by patient cooperation and residual vision.

Choroidal subfoveal thickness (CSFT) was measured manually from the outer boundary of the retinal pigment epithelium (RPE) to the inner scleral border at the highest elevated point of the choroidal lesion utilizing the built-in Heidelberg Eye Explorer (HEYEX) caliper tool (software version 7.0.8.0).

Two independents, masked retinal experts (S.F. and M.D.P.) evaluated the spatial arrangement and qualitative characteristics of specific structural correlates by interpolating en-face NIR/IR findings with corresponding cross-sectional OCT B-scans. Discrepancies in structural grading between the two primary graders were resolved by a third senior supervisor (S.A.).

Statistical Analysis

Statistical processing was performed using JASP (version 0.17.1 (Intel) JASP Team (2023), University of Amsterdam, NL) or RStudio software, version 2022.07.1 (RStudio, PBC, Boston, MA, http://www.rstudio.com/). Continuous variables were assessed for normality using the Shapiro-Wilk test. Normally distributed data were expressed as mean ± standard deviation (mean ± SD), while non-parametric data were expressed as median and interquartile range (median (IQR)). Categorical data were presented as absolute numbers and percentages (%).

Comparative analyses of continuous variables were conducted using the independent-samples t-test for normally distributed variables, or the Mann-Whitney U test for non-parametric datasets. The association between categorical findings was evaluated using Fisher’s exact test. Two-tailed p-values < 0.05 were considered statistically significant.

Results

Of the 17 patients (17 eyes) initially screened, one was excluded due to poor cooperation, resulting in a final analytical cohort of 16 eyes from 16 patients with DCH in SWS. The main characteristics of the study population are summarized in Table 1.

Table 1
Main characteristics of patients with Sturge Weber syndrome

Variables	Study group (N = 16)
Age (years)	26.5 ± 18.3
Gender, female (%)	10 (62.5%)
ETDRS letters, median	37.5 (52)
Glaucoma, n (%)	10 (62.5%)
CSFT, µm	856 ± 450

Quantitative data are expressed as mean ± standard deviation or median (IQR). Choroidal subfoveal thickness (CSFT) at the highest point (micron).

Early Treatment Diabetic Study (ETDRS)

Structural alterations on NIR and OCT B-scan

The most frequent finding was a **granular appearance** seen as hyperreflective dots on both IR and NIR imaging, observed in 13/16 eyes (81.25%) within the posterior pole. A temporal predilection was noted in 5/13 eyes (38.5%), while 8/13 (61.5%) eyes also showed a mid-peripheral involvement. Interpolation between NIR imaging and SDOCT B-scan revealed that hyperreflective dots corresponded to round-to-angular structures in the choriocapillaris near the choroidal lesion (Figs. 1 and 2).

Another finding observed in 6/16 eyes (37.5%) was represented by **inner retinal folds**, visible on fundus examination and NIR as linear striae or folds were appreciated on the perimacular bundle (3/6 cases, 50%) and perifovea (3/6, 50%). This finding correlated on SDOCT B-scan with undulations or irregularities of the internal limiting membrane (ILM) and retinal nerve fiber layer (RNFL) (Fig. 1).

A **demarcation line**, seen as a hyperreflective linear or curved line on NIR, was appreciated in 3/16 eyes (18.75%). On SDOCT B-scan, the RPE profile showed an abrupt elevation caused by the underlying choroidal lesion. This lesion was characterized by a significant increase in CSFT compared to the fellow eye. In these specific cases, the CSFT at its thickest point averaged 1327.7 ± 261.4 µm (range: 1134–1625 µm), whereas the remaining eyes had a significantly lower mean thickness of 747.3 ± 417.0 µm ($p = 0.03$). The demarcation line was appreciated within the posterior pole (2/3 cases, 66.7%) and on mid-peripheral retina in 1/3 case (33.3%). (Figs. 1 and 3) Interestingly, 2/3 eyes (66.7%) with a demarcation line exhibited a pattern resembling **angioid streaks**, with irregular streaks radiating from the optic nerve toward the mid-peripheral retina (Figs. 3 and 4). This association was statistically significant by Fisher's exact test, as none of the eyes without a demarcation line showed this pattern ($p = 0.025$). Those cases featured large, dome-shaped choroidal lesions, one of which was associated with subretinal fluid.

Drusenoid-like lesions were another notable finding, observed with a heterogeneous presentation in 5 out of 16 eyes (31.2%; Fig. 5). These lesions appeared as a diffuse granular hyperreflectivity between the ellipsoid zone (EZ) and the RPE in 2/5 eyes (Case 3, Fig. 5), resembling stage 1 of subretinal drusenoid deposits (SDD)[22]. In one case (Case 1, Fig. 5), pigmentary changes (*yellow arrowhead*) and discrete yellow subretinal lesions (*teal arrowhead*) were seen on color fundus photography. On NIR imaging, these lesions appeared as hyperreflective foci within the macula, extending inferiorly through the posterior pole down to the inferior vascular arcade. Corresponding EDI-SDOCT B-scans revealed a highly thickened choroidal lesion (measuring 1408 µm in height) with overlying subfoveal subretinal fluid and multiple hyperreflective RPE excrescences. In 1/5 cases (20%) (Case 2, Fig. 5), the drusenoid-like lesions were similar to case 1, presenting pigmentary changes (II) and discrete, roundish, subretinal yellow deposits (I), which appeared intensely reflective on IR. On the corresponding SDOCT B-scan, the lesions were seen as focal elevations of the EZ and interdigitation zone/outer segment tips, resembling stage 2 of the SDD classification according to Zweifel et al[22]. In one case, (Fig. 6), yellowish subretinal deposits were evident within the macular region on fundus photography. These deposits corresponded to focal elevations of the RPE and its basal lamina on SDOCT B-scan, confirming the presence of conventional soft drusen. On OCTA, a flow signal in correspondence of a RPE elevation was also appreciated without signs of exudation (Fig. 6, panel C-inset). A summary of the main structural alterations identified in association with DCH is reported in Table 2.

Table 2
Main structural features in eyes with choroidal hemangioma secondary to Sturge Weber syndrome.

Structural Feature	Fundus appearance	NIR/IR imaging	OCT B-scan	Prevalence and clinical significance
Hyperreflective dots	-	Granular appearance with several hyperreflective dots and/or within diffuse hyperreflective area	Round-to-angular structures located specifically in the choriocapillaris near the lesion	81.25% (13/16 eyes). The most frequent finding; often involved the posterior pole with temporal or mid-peripheral predilection
Inner Retinal Folds	Linear striae or folds visible in the perimacular bundle or perifovea	Hyperreflective linear striae or folds	Undulations or irregularities of the internal limiting membrane (ILM) and retinal nerve fiber layer (RNFL)	37.5% (6/16 eyes).
Demarcation line	Not clearly identifiable	Hyperreflective linear or curved line within the posterior pole or mid-periphery	Abrupt retinal pigment epithelium (RPE) elevation due to the mass effect of the choroidal lesion	18.75% (3/16 eyes). Greater choroidal thickness and associated with angioid streaks-like patter radiating from the optic nerve ($p = 0.025$)
Drusenoid-like lesions	Discrete yellowish round lesions. Pigmentary changes	Hyperreflective dots	Diffuse granular hyperreflectivity between the ellipsoid zone and the RPE or RPE elevations in 1 case	31.2% (5/16 eyes). Resembles stage 1 of subretinal drusenoid deposition or reticular pseudodrusen; Only 1 case exhibited conventional drusen

Discussion

This study provides the first detailed characterization of structural remodeling in the outer retina, RPE, and choriocapillaris in eyes with DCH secondary to SWS. Through multimodal imaging interpolation, we identified key structural phenotypes, including granular hyperreflective dots in the choriocapillaris, inner retinal folds (affecting the ILM and RNFL), drusenoid-like lesions, and hyperreflective demarcation lines

(Table 2). Our findings are in line with previous histopathological evidence, demonstrating that the choroidal mass drives structural changes at different anatomical levels[15, 23].

The most ubiquitous microstructural phenotype identified in our cohort was a diffuse granular appearance, manifesting as distinct hyperreflective dots on en-face IR and NIR imaging in 81.25% of eyes. Through direct cross-sectional interpolation with SDOCT B-scans, these hyperreflective round-to-angular structures concentrated within the choriocapillaris layer in correspondence with the primary choroidal lesion. These findings may reflect ultrastructural changes in the RPE and choriocapillaris at the site of a choroidal hemangioma. While the choriocapillaris is generally spared from primary hemangioma infiltration, histopathological specimens revealed varying degrees of secondary degeneration. These alterations include the compression of melanocytic cells toward the sclera and choriocapillaris, sclerosis and obliteration of the choriocapillaris overlying the hemangioma, and focal disruption accompanied by chorioretinal scarring and ossification[14, 23]. The latter tissue alterations were intimately linked to the reactive proliferation and fibrous transformation of the overlying RPE. Furthermore, fibrous nodules arising from the RPE overlying the hemangioma have been described as a hallmark feature, reflecting a characteristic histopathological manifestation of advanced lesions[15, 23]. In Case 1 (Figure 5), hyperreflective excrescences arising from the RPE were prominent, a morphology highly suggestive of nodular fibrosis. This is consistent with the recent consensus from the International Retinal Imaging Society Research (IntRIS) Group, which identifies SDOCT as gold standard for defining fibrosis. On SDOCT, this manifests as homogeneously hyperreflective material with RPE-equivalent reflectivity or as laminated, band-like subretinal material with variable reflectivity on NIR.

NIR imaging uses a longer wavelength (~820–830 nm) that penetrates the neurosensory retina more readily, providing superior contrast and visualization of outer retinal structures, RPE alterations, and the choroid. In our series, the high frequency of these dots (81.25%) invites comparison with neurofibromatosis type 1 (NF1), in which NIR-detected choroidal nodules are a hallmark diagnostic feature. Choroidal nodules appear as hyperreflective round areas on NIR corresponding to a hyperreflective choroidal area on SDOCT B-scan, a finding observed in up to 97% of affected individuals and now considered a key diagnostic criterion. These findings have been attributed to clusters of melanocytes (melanocytic hamartomas) within the choroid[17, 24-27]. However, these NF1-related choroidal nodules differ from the granular appearance observed in our series in terms of reflectivity, size, and topographical localization, suggesting distinct underlying etiologies.

Another finding in our series was inner retinal folds, seen in 37.5% of examined eyes, predominantly in the perifovea and perimacular bundle. This finding has been described in eyes with retinal detachment as partial-thickness folds[28, 29], although the pathogenesis is still poorly understood, this signature may be the result of a mechanical stress from the choroidal mass leading to a retinal deformation, and thus modifications occurring at the vitreoretinal interface. These findings can be easily identified on both clinical and multimodal imaging, facilitating the detection of DCH lesions.

While drusen formation associated with CH has been documented in histopathological specimens, clinical correlates have remained sparse in existing literature[8, 16, 23]. In our series, drusenoid-like lesions were identified and characterized in 31.2% of eyes, manifesting as diffuse granular hyperreflectivity localized between the EZ and the RPE. This peculiar phenotype mirrors the SDD stages on SDOCT B-scan proposed by Zweifel et al[22] and later by Querques et al.[30] SDD, also referred to as reticular pseudodrusen, are typically seen in eyes with age-related macular degeneration (AMD) and hypothesized to originate from pre-existing choroidal hypoperfusion[31-33]. In this regard, hypoxic conditions at the choriocapillaris have been found to disrupt RPE polarity. This leads to preferential apical secretion of apoE into the subretinal space rather than the basal sub-RPE compartment[34, 35], contributing to photoreceptor dysfunction with shortening of outer segments and thinning of the outer nuclear layer. A vascular insufficiency associated with CH is conceivable, given the massive proliferation of vascular channels and cavernous vessels. This vascular environment is likely inefficient due to blood stagnation and impaired oxygen transport to the overlying RPE and outer retina. Therefore, as observed in the SDD pathogenetic model, the local hypoxia may affect RPE cells polarization leading to the accumulation of drusenoid-like material, photoreceptor dysfunction, and ultimately contributing to the visual impairment often observed in these patients.

The least frequent finding in our series was represented by a demarcation line on NIR imaging in 18.75% of eyes. This subgroup had significantly thicker lesions at their highest point (1327.7 ± 261.4 μm) than eyes without a demarcation line (747.3 ± 417 μm, p=0.03). Notably, 66.7% of eyes with a demarcation line also exhibited an irregular, radiating pattern branching from the optic nerve, resembling angioid streaks. Angioid streaks are linear breaks in a calcified Bruch’s membrane observed in pseudoxanthoma elasticum (PXE), a genetic disorder characterized by mutations in ABCC6 gene or ENPP1. In PXE, the elastic fibers in Bruch’s membrane develop calcification with spontaneous breaks[36]. In our series, the combination of extreme choroidal thickening with asymmetric distribution of the choroidal thickness, high tumor volume, and chronic tissue stretching likely causes localized mechanical fractures within Bruch's membrane, mirroring the phenotypic appearance of angioid streaks.

Limitations of the present study include the relatively small sample size, reflecting the rarity of SWS with underlying DCH. Furthermore, factors such as young age, low visual acuity, and comorbidities constrained both data acquisition and imaging quality. Despite these limitations, this study represents the first comprehensive characterization of the structural remodeling of the outer retina, RPE, and choriocapillaris in this population

In conclusion, DCH in SWS is characterized by a distinct spectrum of microstructural alterations, including granular appearance, inner retinal folds, demarcation line, and drusenoid-like deposits. These findings likely result from the chronic mechanical forces exerted by the mass, combined with a functionally inefficient metabolic environment that impairs oxygen transport to the outer retina. Identifying these correlates has dual implications: it advances our understanding of the pathogenic

remodeling occurring in SWS-affected eyes and establishes these structural features as non-invasive biomarkers for earlier detection and monitoring.

Our study highlights the value of high-resolution multimodal imaging interpolation in uncovering the subtle microstructural landscape of DCH in SWS. The identification of choriocapillaris hyperreflective dots, ILM undulations, angioid streak-like demarcation lines, and subretinal drusenoid-like material indicates that these lesions inflict a severe combination of chronic mechanical strain and outer retinal metabolic stress. Recognizing these specific structural correlates enhances our understanding of SWS ocular pathology and may provide crucial surrogate markers for tracking disease chronicity and optimizing visual outcomes before irreversible macular damage occurs.

Declarations

Declaration of competing/conflicts of interest

none

Funding:

This work was supported by Fondazione Telethon and Associazione Italiana Sturge Weber (Grant # GSA22N002).

Author Contribution

SF, GS, SA made substantial contributions to the conception and design of the work, analysis and interpretation of data; MDP, CC, FR made substantial contributions to the acquisition and analysis of data; SF, MDP, CC, FR, SA drafted the work; GS and SA revised it critically for important intellectual content; all authors approved the version to be published and agree to be accountable for all aspects of the work in ensuring that questions related to the accuracy or integrity of any part of the work are appropriately investigated and resolved.

References

1. Hassanpour K, Nourinia R, Gerami E et al (2021) Ocular Manifestations of the Sturge–Weber Syndrome. J Ophthal Vis Res 16:415–431
2. Dingenen E, Segers D, De Maeseneer H, Van Gysel D (2024) Sturge–Weber syndrome: an update for the pediatrician. World J Ped 20:435–443
3. Helmi H, Alkatan H, Al-Essa R et al (2021) Choroidal hemangioma in Sturge Weber syndrome: Case series with confirmed tissue diagnosis. Int J Sur Case Rep ;89

4. Rivasés G, Bakkali IE, De Rivas MO et al (2022) Choroidal haemangioma and its multimodal diagnosis: A case report. Acta Ophthalmol ; 100
5. Silverstein M, Salvin J (2019) Ocular manifestations of Sturge-Weber syndrome. Curr Opin Ophthalmol 30(5):301–305
6. Waelchli R, Aylett SE, Robinson K et al (2014) New Vascular Classification of Port-Wine Stains: Improving Prediction of Sturge-Weber Risk. Br J Dermatol 171(4):861–867
7. Mantelli F, Bruscolini A, La Cava M et al (2016) Ocular manifestations of Sturge-Weber syndrome: pathogenesis, diagnosis, and management. Clin Ophthalmol 10:871–878
8. Abdolrahimzadeh S, Parisi F, Mantelli F et al (2017) Retinal pigment epithelium-photoreceptor layer alterations in a patient with Sturge-Weber syndrome with diffuse choroidal hemangioma. Ophthalmic Genet 38(6):567–569
9. Ciancimino C, Di Pippo M, Rullo D et al (2023) An Update on Multimodal Ophthalmological Imaging of Diffuse Choroidal Hemangioma in Sturge Weber Syndrome. Vision (Basel). ; 6;7(4):64
10. Abdolrahimzadeh S, Fameli V, Mollo R et al (2015) Rare Diseases Leading to Childhood Glaucoma: Epidemiology, Pathophysiogenesis, and Management. Biomed Res Int 2015:781294
11. Abdolrahimzadeh S, Pugi DM, de Paula A, Scuderi G (2021) Ocular manifestations in phakomatosis pigmentovascularis: Current concepts on pathogenesis, diagnosis, and management. Surv Ophthalmol 66(3):482–492
12. Abdolrahimzadeh S, Scavella V, Battaglia D, Recupero SM (2016) Spectral domain optical coherence tomography of choroidal and outer retinal layer thickness in the Sturge Weber syndrome. Curr Eye Res 41(12):1614–1617
13. Abdolrahimzadeh S, Scavella V, Felli L et al (2015) Ophthalmic Alterations in the Sturge-Weber Syndrome, Klippel-Trenaunay Syndrome, and the Phakomatosis Pigmentovascularis: An Independent Group of Conditions? Biomed Res Int 2015:786519
14. Formisano M, di Pippo MC, Scuderi L, Abdolrahimzadeh S (2021) Current concepts on diffuse choroidal hemangioma in Sturge Weber syndrome. Ophthalmic Genet 42(4):375–382
15. Finger PT (2019) Radiation therapy for exudative choroidal hemangioma. Ind J Ophthalmol 67(5):579–581
16. Di Pippo M, Rullo D, Ciancimino C et al (2025) advancing non-invasive ophthalmic imaging in Sturge-Weber syndrome: clinical guidelines towards early choroidal hemangioma detection. J Clin Med 14:19
17. Abdolrahimzadeh S, Ciancimino C, Grassi F et al (2021) Near-Infrared Reflectance Imaging in Retinal Diseases Affecting Young Patients. J Ophthalmol 2021:5581851
18. Sukkarieh G, Lejoyeux R, Lemer Y et al (2023) The role of near-infrared reflectance imaging in retinal disease: A systematic review. Surv Ophthalmol 68(3):313–331
19. Banda H, Shah A, Shah G (2019) Application of wide-field infrared reflectance imaging in retinoschisis, retinal detachments, and schisis detachments. Int J Retina Vitreous ;5

20. Yung M, Klufas M, Sarraf D (2016) Clinical applications of fundus autofluorescence in retinal disease. Int J Retina Vitreous ;2
21. Sparrow J, Duncker T, Schuerch K et al (2019) Lessons learned from quantitative fundus autofluorescence. Prog Ret Eye Res 74:100774
22. Zweifel SA, Spaide RF, Curcio CA et al (2010) Reticular pseudodrusen are subretinal drusenoid deposits. Ophthalmology 117(2):303–312 e1
23. Witschel H, Font RL (1976) Hemangioma of the choroid. A clinicopathologic study of 71 cases and a review of the literature. Surv Ophthalmol 20(6):415–431
24. Viola F, Villani E, Natacci F et al (2012) Choroidal abnormalities detected by near-infrared reflectance imaging as a new diagnostic criterion for neurofibromatosis 1. Ophthalmology 119(2):369–375
25. Moramarco A, Giustini S, Nofroni I et al (2018) Near-infrared imaging: an in vivo, non-invasive diagnostic tool in neurofibromatosis type 1. Graefes Arch Clin Exp Ophthalmol 256(2):307–311
26. Nakakura S, Shiraki K, Yasunari T et al (2005) Quantification and anatomic distribution of choroidal abnormalities in patients with type I neurofibromatosis. Graefes Arch Clin Exp Ophthalmol 243(10):980–984
27. Ueda-Consolvo T, Miyakoshi A, Ozaki H et al (2012) Near-infrared fundus autofluorescence-visualized melanin in the choroidal abnormalities of neurofibromatosis type 1. Clin Ophthalmol 6:1191–1194
28. Dell'Omo R, Mura M, Lesnik Oberstein SY et al (2012) Early simultaneous fundus autofluorescence and optical coherence tomography features after pars plana vitrectomy for primary rhegmatogenous retinal detachment. Retina 32(4):719–728
29. Gupta RR, Iaboni DSM, Seamone ME, Sarraf D (2019) Inner, outer, and full-thickness retinal folds after rhegmatogenous retinal detachment repair: A review. Surv Ophthalmol 64(2):135–161
30. Querques G, Canoui-Poitrine F, Coscas F et al (2012) Analysis of progression of reticular pseudodrusen by spectral domain-optical coherence tomography. Invest Ophthalmol Vis Sci 53(3):1264–1270
31. Li J, Liu Z, Lu J et al (2023) Decreased macular choriocapillaris perfusion in eyes with macular reticular pseudodrusen imaged with swept-source OCT angiography. Invest Ophthalmol Vis Sci ;64
32. Abdolrahimzadeh S, Zweifel SA, Di Pippo M et al (2024) Central macular choriocapillaris impairment as a manifestation of microvascular disease in eyes with subretinal drusenoid deposits. Eye (Lond) 38(1):173–178
33. Alten F, Clemens CR, Heiduschka P, Eter N (2013) Localized reticular pseudodrusen and their topographic relation to choroidal watershed zones and changes in choroidal volumes. Invest Ophthalmol Vis Sci 54(5):3250–3257
34. Digsby K, Zhang Q, Miller JML (2025) Basic science observations link subretinal drusenoid deposit formation to retinal pigment epithelial hypoxia. Eye (Lond) 39(4):790–792

35. Curcio CA, Goerdt L (2025) A cell culture system for RPE hypoxia, a physiologic stressor relevant to AMD deposit formation. Eye (Lond) 39(4):611–612
36. La Rosa A, Feo A, Bousquet E et al (2026) Angioid streaks-related choroidal neovascularization: Clinical features, multimodal imaging-based differential diagnosis, and optimized treatment strategies. Surv Ophthalmol 71(2):309–320

Figures

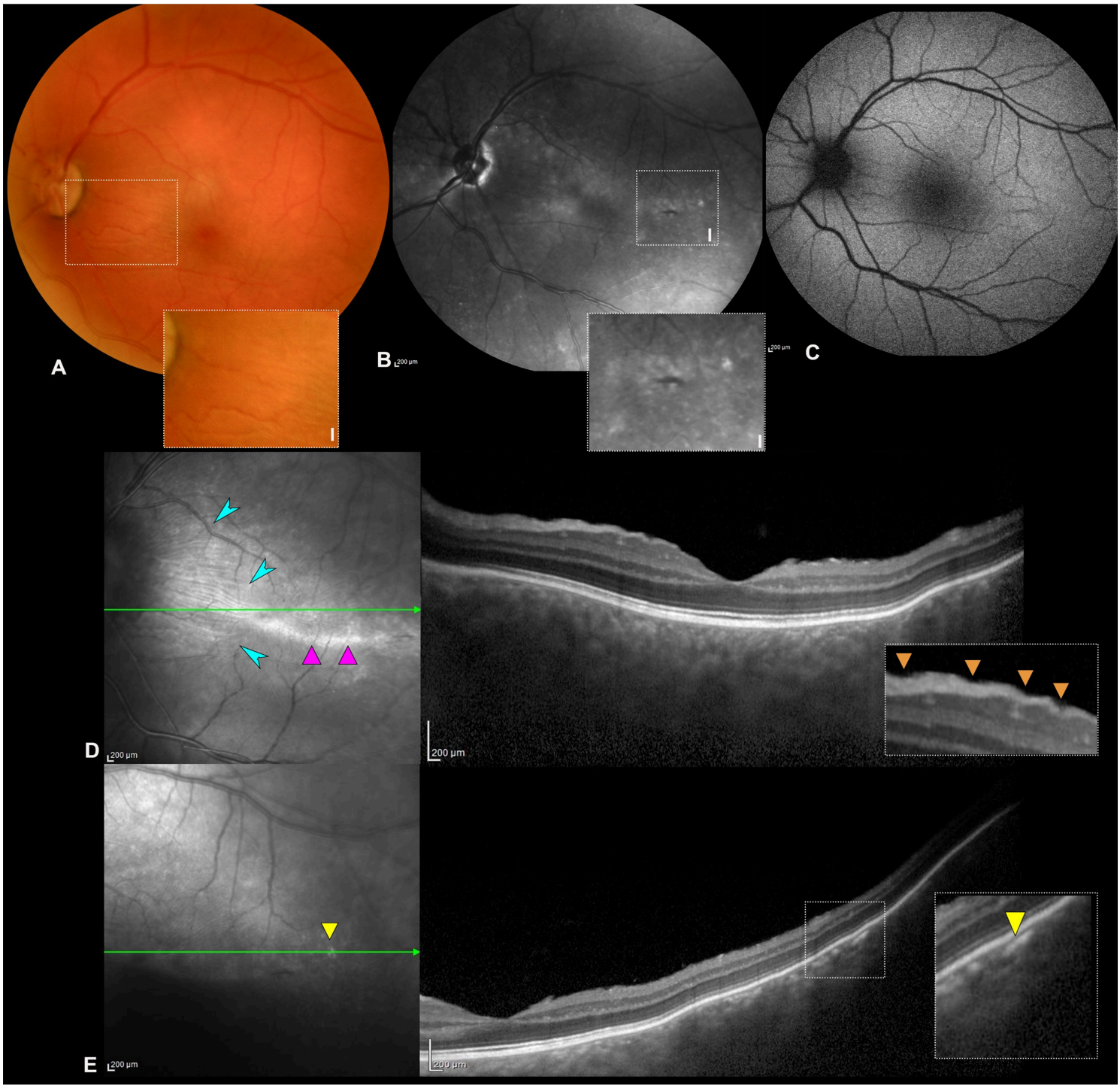


Figure 1

Exemplary case of microstructural alterations seen in diffuse choroidal hemangioma secondary to Sturge-Weber syndrome. A, Color fundus photograph shows a diffuse orange discoloration within the posterior pole and the presence of retinal folds, better seen on magnification. B, Infrared shows roundish multiple hyperreflectivities particularly on the temporal side. C, Fundus autofluorescence (FAF) demonstrates no relevant findings. D, Near infrared reflectance (NIR) shows both inner retinal folds (teal arrowheads) and a demarcation line (purple triangles). On the corresponding optical coherence tomography (OCT) B-scan the inner retinal folds appear as undulations or irregularities of the inner limiting membrane and retinal nerve fiber layer. E, NIR and spectral domain optical coherence tomography B-scan passing through the hyperreflective dots shows hyperreflective round to polygonal hyperreflectivity seen within the choriocapillaris.

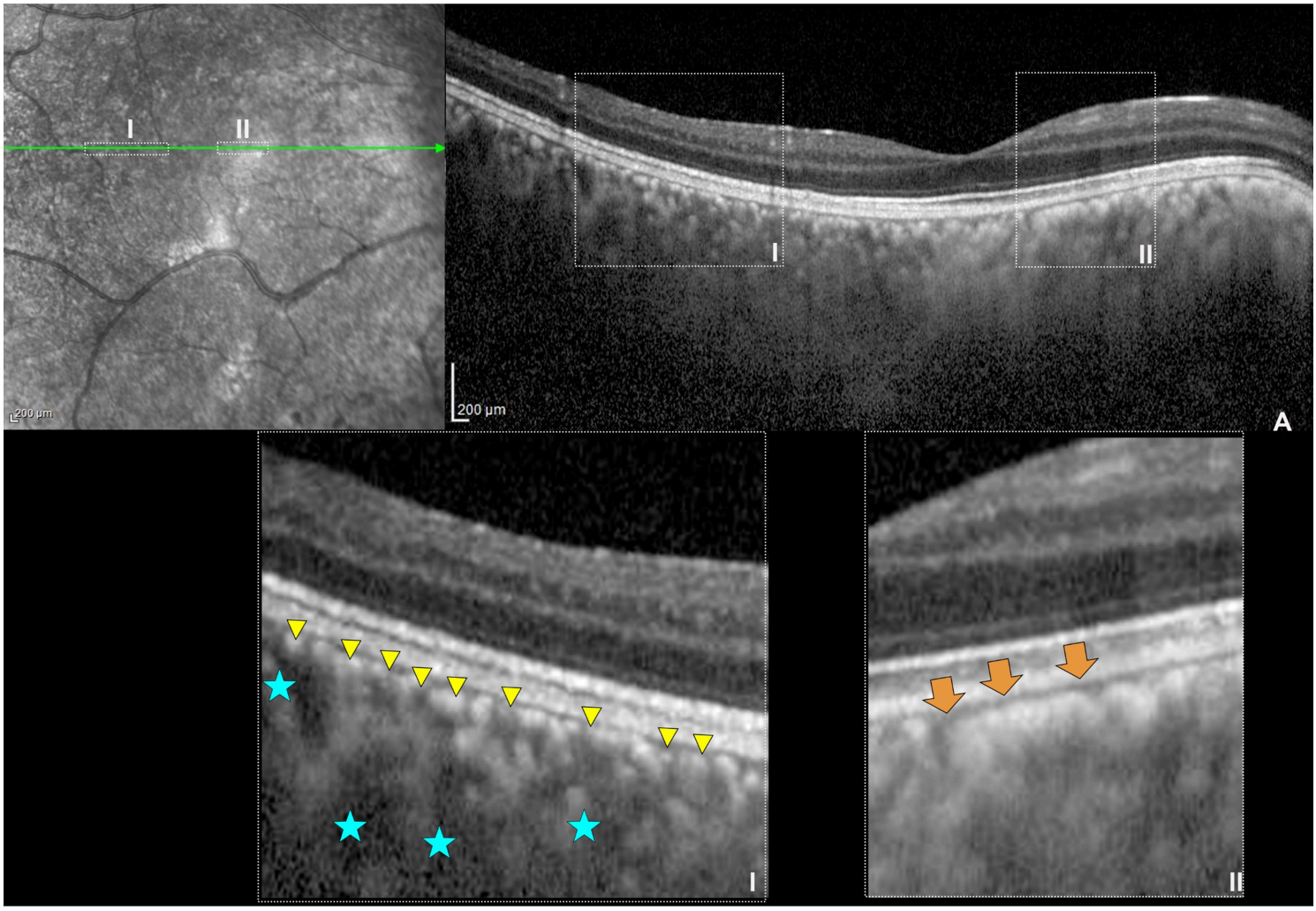


Figure 2

Hyperreflective dots on near infrared reflectance (NIR) and spectral domain optical coherence tomography (SDOCT). A, Fine hyperreflective dots are visible on NIR (I) corresponding on SDOCT B-scan (AI) to round-to-angular structures located specifically in the choriocapillaris (yellow triangles) vascular lumens beneath these findings can be appreciated (teal arrowheads). The hyperreflective diffuse

granularity on NIR accompanied by diffuse hyperreflectivity (I), corresponding to diffuse hyperreflective plaques on SDOCT B-scan.

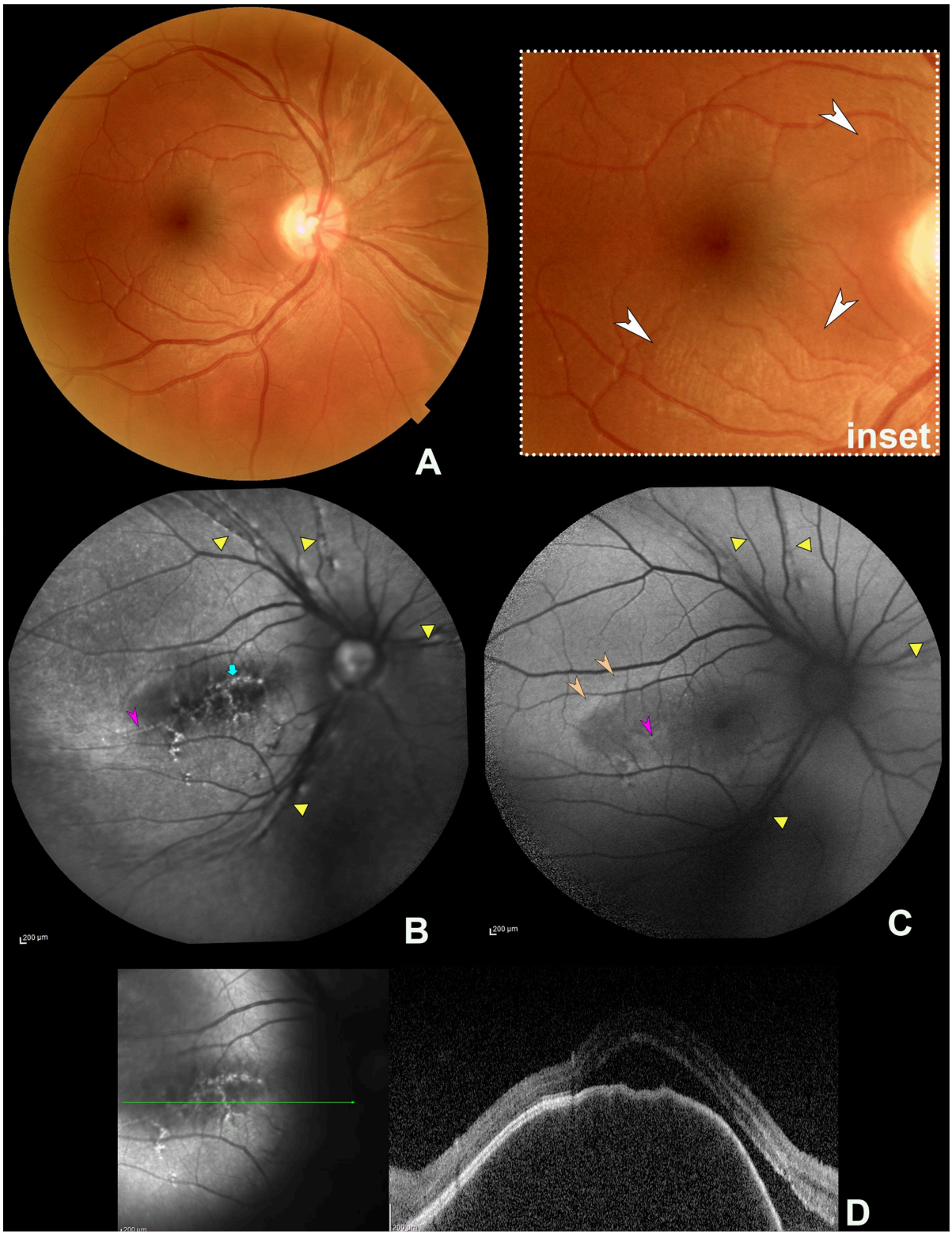


Figure 3

Exemplary case of microstructural alterations seen in diffuse choroidal hemangioma secondary to Sturge-Weber syndrome. A, Color fundus photograph showing inner retinal folds, better seen on

magnification (*white arrowheads*). B, Infrared shows a demarcation line (purple triangle), irregular pattern-like hyperreflective lesions on posterior pole (teal arrow). Moreover, irregular streaks radiating from the optic nerve toward the mid-peripheral retina can be appreciated (yellow triangles). C, Fundus autofluorescence showing hyperautofluorescence surrounding a central hypoautofluorescence (peach arrowheads), while a thin hyperautofluorescent line can be recognized (purple arrowhead). D, Near infrared reflectance confirms the presence of a pattern-dystrophy like appearance on posterior pole while the spectral domain optical coherence tomography B scan shows a large dome-shaped choroidal lesion with subretinal fluid.

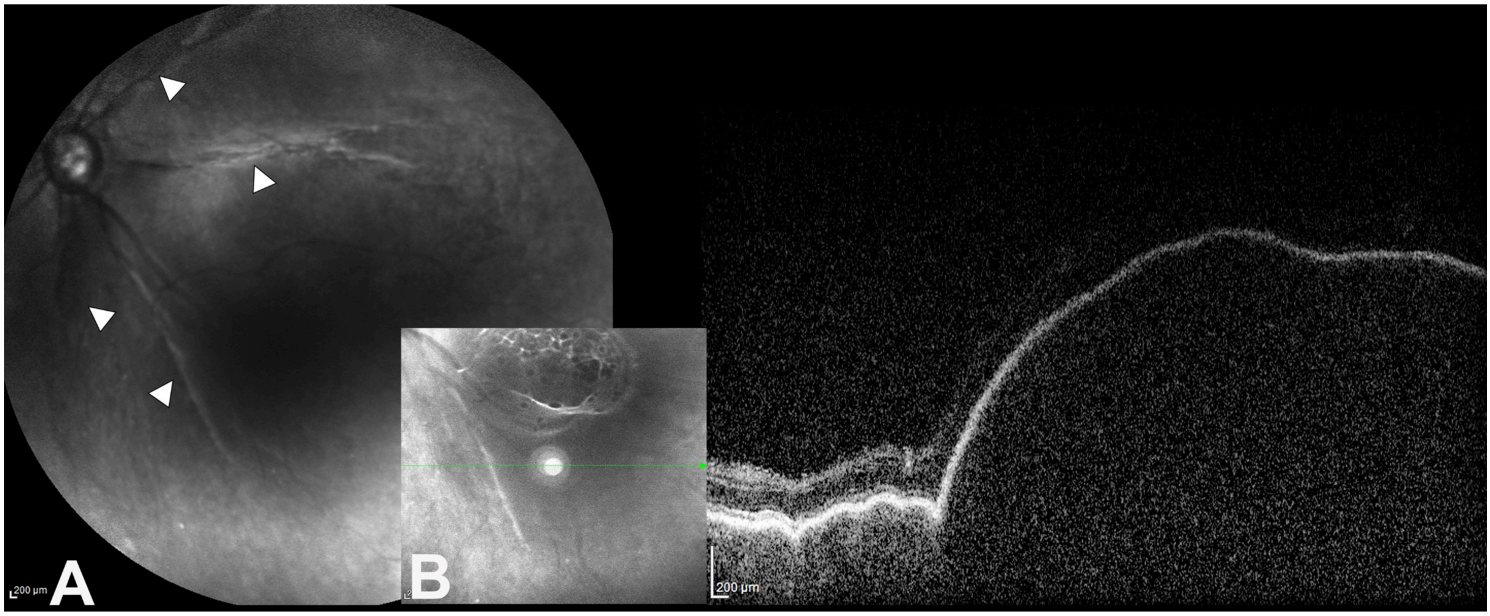


Figure 4

Angioid streaks like appearance in diffuse choroidal hemangioma secondary to Sturge-Weber syndrome. A, Infrared shows multiple hyperreflective lines radiating from the optic nerve (white triangles). B, spectral domain optical coherence tomography B-scan reveals an irregular profile of the retina for the presence of a large dome-shaped choroidal mass.

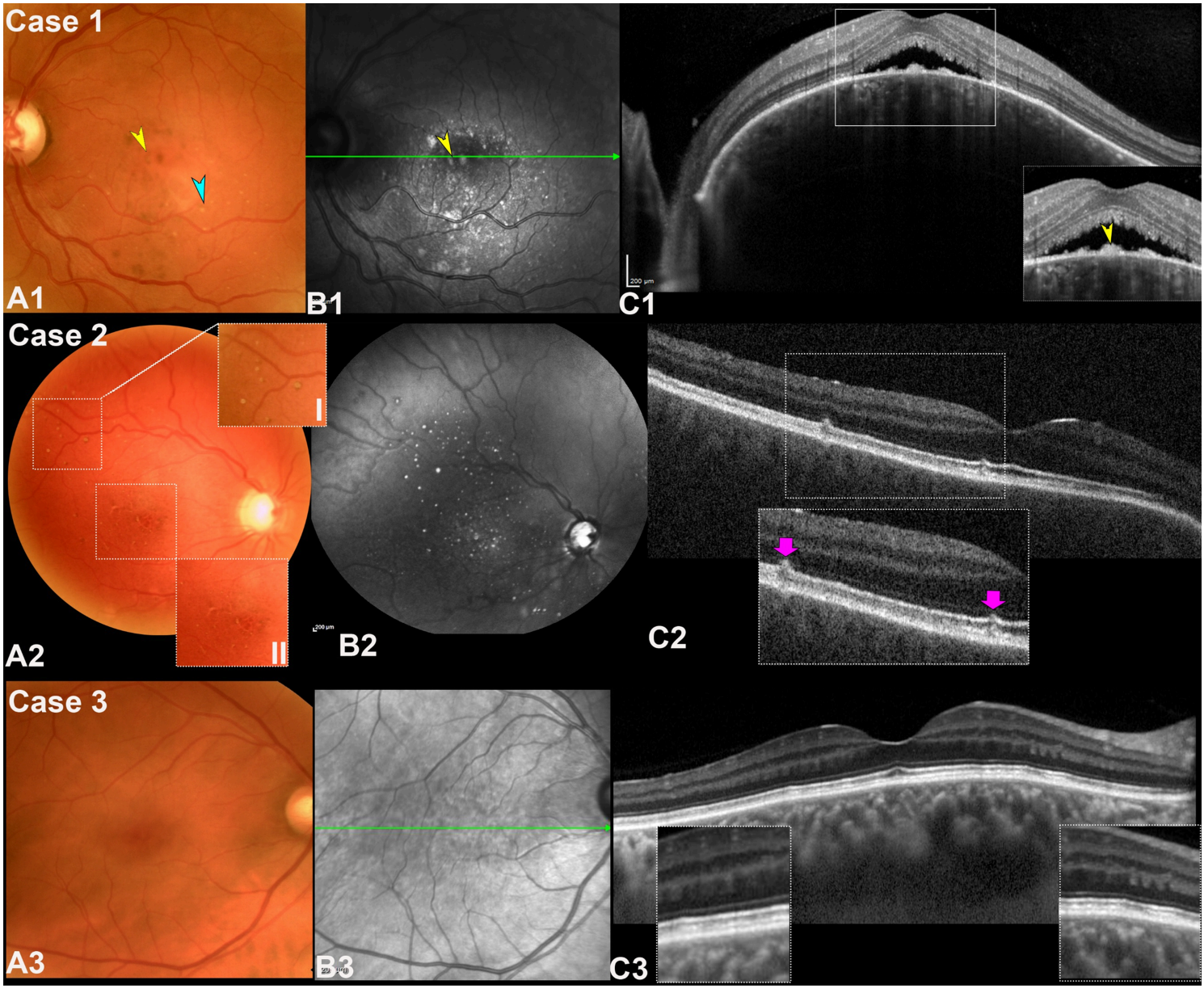


Figure 5

Multimodal imaging features of drusenoid-like lesions in eyes with diffuse choroidal hemangioma associated with Sturge–Weber syndrome.

Case 1: Color fundus photography (A1) shows pigmentary alterations (yellow arrowhead) and discrete yellowish subretinal deposits (teal arrowhead). Near-infrared reflectance imaging (B1) demonstrates multiple hyperreflective foci extending across the posterior pole. The green line indicates the location of the corresponding spectral domain optical coherence tomography (SDOCT) B-scan (C1), which reveals marked choroidal thickening due to the underlying hemangioma, subfoveal subretinal fluid, and hyperreflective retinal pigment epithelium (RPE) excrescences, highlighted in the magnified inset (yellow arrowhead).

Case 2: Color fundus photography (A2), with magnified insets, shows multiple discrete, round, yellowish subretinal deposits (inset I) and pigmentary alterations (inset II). These lesions appear as intensely

hyperreflective on infrared imaging (B2). The corresponding SDOCT B-scan (C2) demonstrates focal elevations of the ellipsoid zone and interdigitation zone/photoreceptor outer segment tips (magenta arrows in the magnified inset), resembling stage 2 subretinal drusenoid deposits.

Case 3: Color fundus photography (A3) shows subtle mottling of the posterior pole. Near-infrared reflectance imaging (B3) demonstrates a diffuse granular appearance; the green line indicates the location of the corresponding SDOCT scan. The SDOCT image (C3) and magnified insets reveal diffuse granular hyperreflective material between the ellipsoid zone and the RPE, resembling stage 1 subretinal drusenoid deposits.

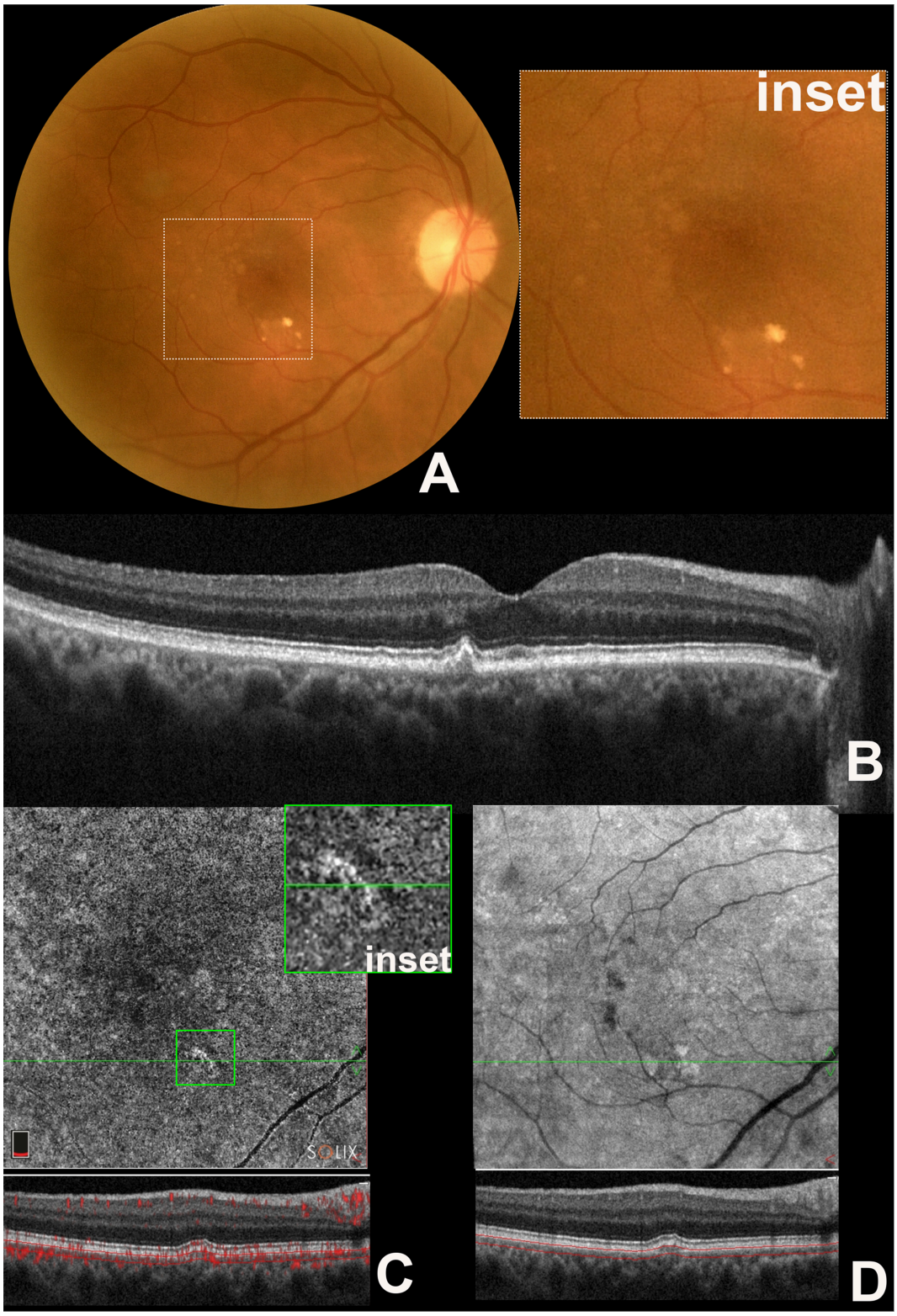


Figure 6

Multimodal imaging of conventional drusen in an eye with diffuse choroidal hemangioma associated with Sturge–Weber syndrome. (A) Color fundus photography shows several yellowish deposits within the macular region, enlarged in the inset. (B) Spectral-domain optical coherence tomography demonstrates a focal elevation of the retinal pigment epithelium and its basal lamina, consistent with a conventional soft druse. (C) En-face optical coherence tomography angiography (OCTA), with magnified inset, reveals a

focal flow signal corresponding to the RPE elevation; the cross-sectional OCTA flow overlay confirms vascular flow at the same location. (D) Corresponding structural en-face OCT and cross-sectional B-scan demonstrate the same RPE elevation without associated intraretinal or subretinal fluid.